An Integrated Switched Reluctance Motor Drive Topology with Voltage-Boosting and On-Board Charging Capabilities for Plug-In Hybrid Electric Vehicles (PHEVs)

Mingyao Ma, *Member, IEEE,* Zhongyi Chang, Yihua Hu, *Senior Member, IEEE,* Fei Li, *Member, IEEE,* Chun Gan, *Member, IEEE*, Wenping Cao, *Senior Member, IEEE*

***Abstract*-- This paper presents a new topology of switched reluctance motor (SRM) drive for plug-in hybrid electric vehicles (PHEVs). Six operating modes can be achieved as a result. Three of those modes are applied for driving and the others for charging. During the driving mode, the topology can be converted to a four-level one. During the charging mode, two battery packs are charged in parallel with the boost circuit by the external AC source or generators. The main contributions of the proposed topology are as follows: 1) A four-level converter is formed by adopting different ways of connection (series or parallel) of the two battery packs (or the two capacitors), which can accelerate the excitation and demagnetization procedures of SRMs. Moreover, the topology contributes to decreasing the switching losses and extending the constant torque region to improve the drive performance as well. 2) The state of charge (SOC) of the two battery packs (or the voltages of two capacitors) can keep balance on their own by parallel operation of the two battery packs. Furthermore, a detailed comparison between two drive modes of the proposed topology and asymmetric half bridge inverters is undertaken with simulation and experimental studies, the results of which demonstrate the validity of the proposed topology.**

***Index Terms*—Fast excitation and demagnetization, plug-in hybrid electric vehicle (PHEV), switched reluctance motor (SRM), battery chargers, switch capacitor, voltage boosting.**

I. Introduction

Electric vehicles (EVs) have been rapidly developed globally as they are cleaner and more efficient than conventional internal combustion engine (ICE) cars [1]-[5]. In EV applications, there are several challenges hampering the wide acceptance of EVs on the marketplace. One is the range anxiety and the other is charging time. Plug-in hybrid electric vehicles (PHEVs) can adopt conventional fossil fuels and electricity as the power source so as to eliminate the range anxiety issue. However, current battery charging technology relies on the use of off-board charging stations which take up urban space and need significant investments. Despite an on-board charging capacity, this is very limited and the charging time is generally long. In theory, it is possible to utilize the machine winding as a charging inductor so as to accelerate the charging process. In literature, different types of electrical machines have been considered for EVs [7]-[10]. Among these machines, switched reluctance motors (SRMs) receive much attention as they have a simple and rugged rotor, and an extended speed range [11]-[13], making them a good candidate for EV applications.

The performance of SRM is subjected to the power source. For example. The maximum output torque increases with the demagnetization voltage, which reduces phase currents after the aligned position [14]. While the motor is supplied by a high voltage at low speeds, the switching frequency needs to increase. This gives raise to switching losses. When the supply voltage is low at high speeds, the output torque is low.

However, the excitation and demagnetization voltages are limited by the supply voltage in conventional SRM drives [15]. Given the availability of energy storage and a limited space envelop in PHEVs, the integration of the multi-level converter and energy storage systems is very practical and effective [16]-[19].

In order to reduce the current rising/falling time and adopt different operation eventuality, some boost converters have been developed [20]-[22]. Typically these topologies attempt to reduce the number of power switches and increase the power levels [23]-[27]. A passive boost capacitor has been added to increase the demagnetization voltage [28]. It is added to the front end of a conventional asymmetric converter, and the current falling time is reduced. However, the current rising time is difficult to reduce because the excitation voltage is generally supplied by the DC-link voltage. An attempt [29] uses a capacitor as energy storage to increase the phase voltage. It can go higher than the supply voltage but the current must flow back to the source during energy return, which decreases the converter efficiency. Meanwhile, the commutation loss increases with the supply voltage. An improved C-dump converter is reported in [30]. It is effective in the utilization of standard converters for higher power and wider speed range of motor drives but the capacitor voltage is difficult to control. In [31], a new versatile converter is presented by integrating the converter, motor with the charger. There are several operating modes for this converter to control the power flow. When driving the motor, it works as a Miller converter.

In this paper, a new topology is presented by integrating a boost circuit, a switch capacitor with two energy storage systems, battery packs and an SRM. It can provide many operation modes, and different ways of connection (series or parallel) for the two battery packs (or two capacitors). The supply voltage can be enhanced, and the state of charge (SOC) of the two battery packs (or the voltages of two capacitors) can be balanced by controlling the circuit in different operation modes.

This paper is organized as follows: In section II, the operating principle of SRM drives is analyzed in detail. In addition, the proposed integrated topology for PHEV is presented. In section III, the control scheme of the proposed integrated multilevel converter is proposed; the operating modes and the current and voltage are analyzed accordingly; the advantages obtained by applying the front-end circuit are presented. The simulation and experimental results are presented in section IV. Finally, conclusions are given in section V.

II. Proposed Integrated Topology

The asymmetric half bridge converter is a popular converter topology in the applications of SRM drives, which consists of two power switches and two diodes in each phase [32]-[34]. Fig. 1 shows a typical asymmetric half bridge converter configuration, where each phase is independent controlled.

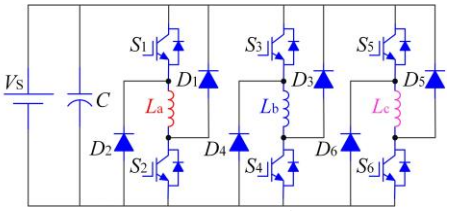

Fig. 1. Three-phase asymmetric half bridge converter.

The per-phase voltage can be expressed as

$$v_k = R_k i_k + \frac{d\lambda(i_k,\theta)}{dt} = Ri_k + \frac{\partial\lambda(i_k,\theta)}{\partial i_k}\frac{di_k}{dt} + \frac{\partial\lambda(i_k,\theta)}{\partial\theta}\frac{d\theta}{dt} \quad (1)$$

where R_k represents the winding resistance and λ (i_k, θ) is the flux linkage of the kth phase. i_k is the phase current of the kth phase, where $k = a, b, c$. θ indicates the rotor position relative to the stator.

If the voltage drop across the power switches and diodes is ignored, the exciting voltage is equal to the supply voltage V_s and the demagnetized voltage is $-V_s$.

The phase incremental inductance l and back-EMF e_k are

$$l = \frac{\partial\lambda_k(i_k,\theta)}{\partial i_k} \quad (2)$$

$$e_k = \frac{\omega\partial\lambda_k(i_k,\theta)}{\partial\theta} \quad (3)$$

Substitute (2) and (3) into (1), the following equation is derived.

$$\frac{di_k}{dt} = (v_k - R_k i_k - e_k)/l \quad (4)$$

The mechanical equations are

$$T_e - T_L = J\frac{d\omega}{dt} \quad (5)$$

$$\omega = \frac{d\theta}{dt} \quad (6)$$

where T_e is the electromagnetic torque, T_L is the load torque and ω is the angular speed.

The electromagnetic torque is calculated by

$$L_k(i_k,\theta) = \frac{\lambda_k(i_k,\theta)}{i_k} \quad (7)$$

$$T_e = \frac{1}{2}\sum_k i_k^2\frac{\partial L_k(i_k,\theta)}{\partial\theta} \quad (8)$$

where $L_k(\theta, i_k)$ is the inductance of the kth phase. When the partial derivative of $L_k(\theta, i_k)$ with respect to θ is positive, T_e is positive, and under this situation the motor works in energy regeneration mode.

The instantaneous electrial power $v_k i_k$ is:

$$v_s i_k = Ri_k^2 + \omega T_e + \frac{d}{dt}(\frac{1}{2}L_k(i_k,\theta)i_k^2) \quad (9)$$

According to the above analysis, the motor performance is closely related to the phase voltage. However, the terminal voltage of each phase is limited by the supply voltage.

This paper proposes an integrated topology for PHEVs, as shown in Fig. 2. It includes an AC generator (G), a diode bridge rectifier (R_E), a DC-link capacitor (C), an inductor L_s, a power switch T_c, a diode D_c, an asymmetric half-bridge converter, two identical capacitors C_1 and C_2 and two battery packs B_1 and B_2. When B_1 and B_2 operate in parallel, their voltages are identical, contributes to achieving identical SOC of the two battery packs. Therefore, a dynamic balance of the dc-link capacitor voltage of the two battery packs can be achieved. The drive torque is then provided by the AC generator (G) or battery packs at drive modes. Moreover, the three relays (J_1, J_2, and J_3) and two diodes (D_u and D_d) are added to increase the functionality at different modes.

Fig. 3 displays the power flow in the drive involving the generator, battery packs, SRM, and an AC source for motoring and charging modes. The generator is mechanically coupled with a small ICE to generate a three-phase power supply. The power is then converted into DC one by a three-phase state of relays J_1, J_2 and J_3 and different drive loads. The PHEV can operate in four driving modes and two charging modes.

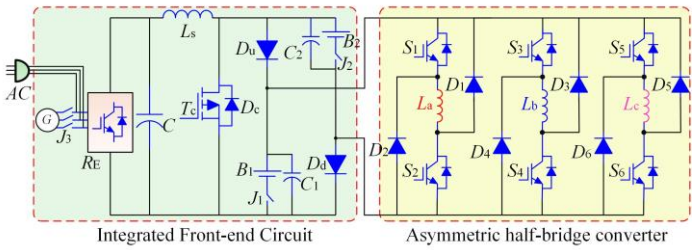

Fig. 2. Proposed three-phase SRM drive.

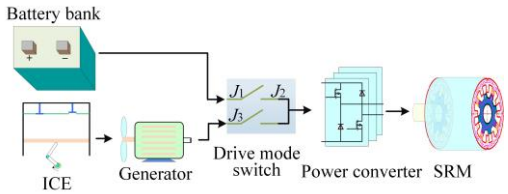

(a) Motoring mode

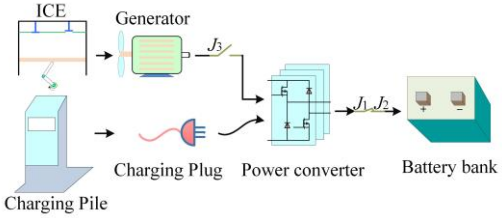

(b) Charging mode

Fig. 3. Power flow chart in two modes.

As is shown in Fig. 3(a), the four driving modes include the generator-alone drive mode, battery-alone driving mode, hybrid driving mode and generator charging mode. As is presented in Fig. 3(b), the battery is charged by the generator or the power supply.

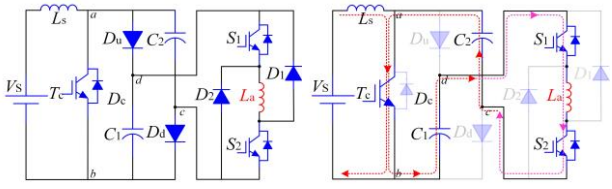

(a) Configuration at the generator-alone (b) Two capacitors series excitation

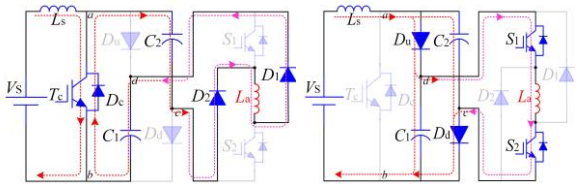

(c) Two capacitors series demagnetization (d) Two capacitors parallel excitation

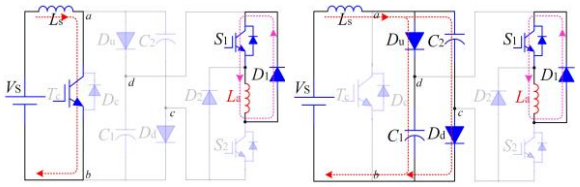

(e) Two capacitors parallel freewheeling mode1 (f) Two capacitors parallel freewheeling mode 2

Fig. 4. Configuration of the generator-alone drive and its operation modes.

A. *Generator-alone Driving Mode*

When J_1 and J_2 are open and J_3 is closed, the generator provides power to the SRM, as is shown in Fig. 3(a). The effective circuit is illustrated in Fig. 4(a). It consists of a boost circuit, a switch capacitor circuit and an asymmetric converter. The combination of the ICE and generator is simplified as a power source with V_s. Compared with the conventional asymmetric converter, the proposed converter has one more switch, capacitor, and inductor, and two additional diodes. Switch *Tc* and diode D_c can be replaced by a power switch with an anti-parallel diode. While the two capacitors are connected in parallel, the *dc* terminal voltage is equal to the *ab* output voltage. If the two capacitors are connected in series, the output voltage could be twice the *ab* voltage.

The proposed converter can operate in five modes: two capacitor series excitation, two capacitor series demagnetization, two capacitor parallel excitation, two capacitor parallel freewheeling mode 1, and two capacitor parallel freewheeling mode 2. These are depicted in Fig. 4(b)-(f) taking phase A as an example.

Mode 1: The converter operates with two capacitor series excitation, as shown in Fig. 4(b). In this mode, diodes D_1, D_2, D_u, D_d and D_c are reversely biased. *Vs* is powered by *G*. Phase winding *La* is excited by C_1 and C_2 (connected in series). The current flows through C_1, C_2, *Tc*, S_1, and S_2. Meanwhile, V_s charges *Ls* by *Tc*. The voltage and current can be expressed as:

$$V_{ab} = 0 \tag{11}$$

$$V_{dc} = V_{c1} + V_{c2} - V_t \tag{12}$$

$$V_A = V_{c1} + V_{c2} - 3V_t = R_a i_a + L_a(\theta)\frac{di_a}{dt} + i_a\omega\frac{dL_a(\theta)}{d\theta} \tag{13}$$

$$I_A = -I_{c1} = -I_{c2} \tag{14}$$

where V_{dc} is the *dc* voltage, V_{C1} and V_{C2} are C_1 and C_2 voltages, respectively, V_t is the voltage drop of the power switch, V_{ab} is the *ab* voltage, and I_{C1} and I_{C2} are C_1 and C_2 currents, respectively.

Mode 2: The converter operates in two capacitor series demagnetization, as shown in Fig. 4(c). L_s is charged by V_s. C_1 and C_2 are connected in series by D_c. S_1 and S_2 are open. The two capacitors are charged by D_u, D_d and D_c. The voltage and current of phase A are given by

$$V_{ab} = 0 \tag{15}$$

$$V_{dc} = V_{c1} + V_{c2} - V_d \tag{16}$$

$$V_A = -V_{c1} - V_{c2} - 3V_d = R_a i_a + L_a(\theta)\frac{di_a}{dt} + i_a\omega\frac{dL_a(\theta)}{d\theta} \tag{17}$$

$$I_A = I_{c1} = I_{c2} \tag{18}$$

where V_d is the voltage drop across the diode.

Mode 3: The converter operates in two capacitor parallel excitation, as shown in Fig. 4(d). C_1 and C_2 are connected in parallel by D_1 and D_2. *Tc* is switched off while S_1 and S_2 are closed. The two capacitors are charged by V_s and *Ls*, and the phase winding *La* is energized by C_1 and C_2 (connected in parallel). Therefore, the two capacitor voltages are identical, and the SOC of the two battery packs can be dynamically balanced when employing this mode. Assume the capacitances of C_1 and C_2 are identical, and the C_1 and C_2 voltage are *Vc*. The voltage and current equations of phase A are given by

$$V_{ab} = \frac{T}{t_{off}}DV_s \tag{19}$$

$$V_{dc} = V_{ab} - V_d \tag{20}$$

$$V_A = V_c + 2V_t - V_d = V_{ab} - V_d = R_a i_a + L_a(\theta)\frac{di_a}{dt} + i_a\omega\frac{dL_a(\theta)}{d\theta} \tag{21}$$

$$I_A = I_s - I_{c1} - I_{c2} \tag{22}$$

where *T* is the switching period of *Tc*, t_{off} is the off time when *Tc* is turned off. D is the duty cycle and I_s is the supply current.

Mode 4: The converter operates in two capacitor parallel freewheeling mode 1, as shown in Fig. 4(e). Only one power switch S_1 turns on. Hence, the phase current flows through S_1 and D_u. At the same time, *Ls* is charged by V_s. The voltage and current of phase A are zero.

$$V_{ab} = 0 \tag{23}$$

$$V_A = 0 \tag{24}$$

Mode 5: The converter operates in two capacitors parallel freewheeling mode 2, as shown in Fig. 4(f). C_1 and C_2 are connected in parallel and they are charged by the boost circuit separately. The SOC of the two battery packs can be dynamically balanced. The phase current flows through D_u and S_1. The voltage equations of phase A are given by

$$V_{ab} = \frac{T}{t_{off}}DV_s \tag{25}$$

$$V_{dc} = V_{ab} - V_d \tag{26}$$

$$V_A = 0 \tag{27}$$

B. Battery-alone Drive Mode

When J_1 and J_2 are closed and J_3 is open, the battery drives the SRM, as presented in Fig. 5(a). *Tc* and diode D_c can be replaced by a power switch with an anti-parallel diode.

This converter has five operating modes, including two capacitor series excitation, two capacitor series demagnetization, freewheeling mode, two capacitor parallel excitation mode 1, and two capacitor parallel excitation mode 2, as shown in Fig. 5(b)–(f). If the voltage drop across the power switches and diodes is ignored, the phase voltage is equal to the *ab* output voltage. In essence, the connection of C_1 and B_1 in parallel is identical to that of C_2 and B_2 in parallel. The voltages of C_1 and C_2 are assumed as *Vc*.

In two capacitors series excitation mode shown in Fig. 5(b), *La* is energized. S_1 and S_2 are turned on, and the excitation energy is from B_1 and B_2. *Tc* is turned on, and C_1 and C_2 are connected in series by *Tc*. The phase voltage is given by

$$V_A = 2V_c = R_a i_a + L_a(\theta)\frac{di_a}{dt} + i_a\omega\frac{dL_a(\theta)}{d\theta} \tag{28}$$

When the converter operates in two capacitors series demagnetization mode, the circuit and power flows are shown in Fig. 5(c), *La* is demagnetized. S_1 and S_2 are turned off and the recovered energy from *La* is fed to the switch capacitor. The two capacitors are connected in series by diode D_c.

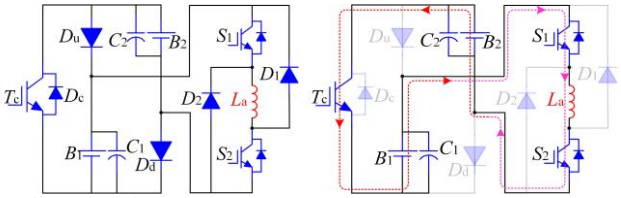

(a) Configuration of the battery-alone drive (b) Two capacitors series excitation

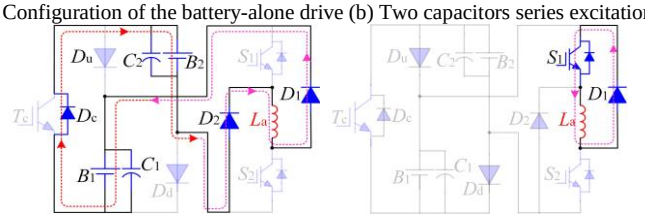

(c) Two capacitors series demagnetization (d) Freewheeling mode

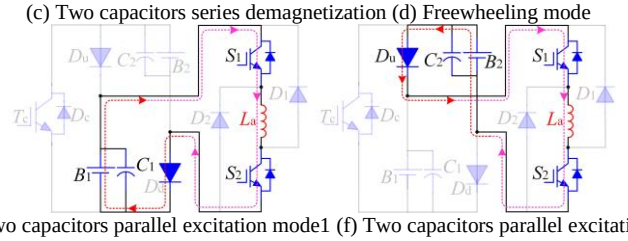

(e) Two capacitors parallel excitation mode1 (f) Two capacitors parallel excitation mode2

Fig. 5. Configuration of the battery-alone drive and its operation modes.

The demagnetization current flows through D_1, D_2, and D_c to charge C_1 and C_2. The phase voltage is given by

$$V_A = -2V_c = R_a i_a + L_a(\theta)\frac{di_a}{dt} + i_a\omega\frac{dL_a(\theta)}{d\theta} \tag{29}$$

The converter operates in freewheeling mode, as in Fig. 5(d). Only one power switch S_1 is turned on, the phase current flows through D_1, S_2 or D_2, S_1. The phase voltage is zero.

While S_1 and S_2 are turned on, *La* is energized. Because *Tc* is turned off, the two capacitors and two diodes that compose of the two independent voltage sources are connected in parallel. The energy is supplied by one of the two capacitors. This is determined by the voltage level of the two capacitors. A dynamic balance of the SOC of the two battery packs can be achieved in this mode. The two capacitor parallel excitation mode 1 and mode 2 are shown in Fig. 5(e) and (f). The voltage of phase A is given by

$$V_A = V_c = R_a i_a + L_a(\theta)\frac{di_a}{dt} + i_a\omega\frac{dL_a(\theta)}{d\theta} \tag{30}$$

C. Hybrid Drive Mode

When J_1, J_2 and J_3 are closed, the SRM is powered by the generator and the two battery packs, as shown in Fig. 3(a). The PHEV operates in the hybrid drive mode. Compared with the generator-alone drive mode, two additional battery packs B_1 and B_2 are added in the hybrid drive mode. Therefore, the battery packs drive the SRM together with the generator at heavy loads.

D. Generator Drive Charging Mode

When J_1, J_2 and J_3 are closed, the generator drives the SRM and charges the two battery packs at the same time. As is shown in Fig. 3(a), the PHEV operates in the generator drive charging mode. This is for light-load operation.

E. Battery Charge By an External Power Source

When J_1 and J_2 are closed and J_3 is open, the battery packs are charged by an external source, as is shown in Fig. 6. A boost circuit is formed. By controlling the power switch *Tc*, B_1 and B_2 can be charged in parallel by a boost voltage.

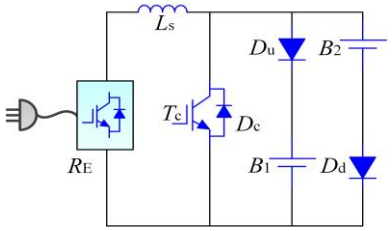

Fig. 6. Battery charging mode.

F. Battery Charge By Generator

When J_1, J_2 and J_3 are turned on, the battery packs are charged by the generator, as shown in Fig. 3(b). In comparison to the battery charged by an external power source, the source power of this mode is charged by a generator.

III. Control Scheme for the Proposed Topology

The control strategy of the converter under drive modes is illustrated in Fig. 7. θ_{on} is the turn-on angle and θ_{off} is the turn-off angle. Δi is the current hysteresis loop width, i_a, i_b and i_c are the three-phase currents for phases A, B and C, respectively. ω^* is the speed reference. The angle and instantaneous speed can be measured experimentally. According to the drive modes, the proposed topology can operate in the generator-alone charging mode, battery-alone drive mode, hybrid drive mode, and generator drive charging mode. The drive control should consider the overlap current, turn-on and turn-off angles, phase current, and motor speed. The current reference i^* is generated by a PI controller with the speed error, and the drive signal of the topology is generated from a current hysteresis controller and a commutation controller. The three-phase currents are detected by current sensors, and fed back to the current hysteresis controller by an A/D controller. The current hysteresis controller can regulate the amplitudes of the phase currents. The turn-on and turn-off angles are determined by the rotor position to control the phase commutation. The converter drives the SRM by the switch signals from the commutation controller.

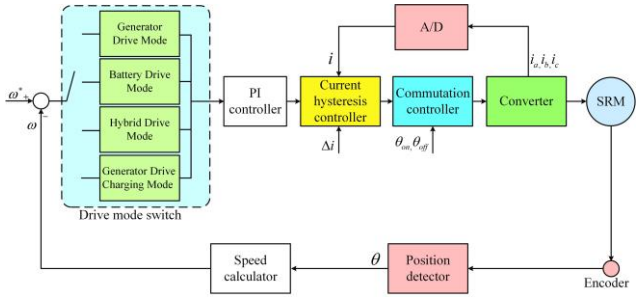

Fig. 7. Control strategy under drive modes.

In this paper, a current overlap situation is analyzed. As is shown in Fig. 8, the current overlap of two phases can be divided into two cases according to the turn-on angle of the incoming phase and the turnoff angle of the outgoing phase. In Fig. 8(a), the conducting intervals of the incoming phase and output phase are

not overlapped. The phase voltage is equal to the *ab* voltage and the voltages of C_1 and C_2 are equal to *Vc*.

In interval 1, C_1 and C_2 are connected in series, S_1 and S_2 are turned on at θ_{on} and 2*Vc* is applied across the load. This interval is denoted as the initial excitation interval. In interval 2, the positive current ramp reaches the upper limit. One of S_1 and S_2 is turned off. The circuit is in freewheeling mode and the phase voltage is zero. There are two cases in freewheeling mode

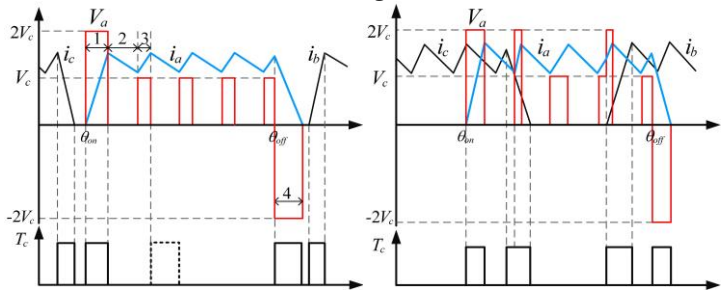

(a) Conduction angle<=120 (b) 180>=conduction angle>120

Fig. 8. The waveform of phase voltage, current and conduction angle state.

In interval 3, the current reaches the lower level and *Vc* is applied by turning on both the two switches. C_1 and C_2 are connected in parallel. At the rotor position θ_{off}, both switches are turned off and -2*Vc* is applied across the load, and the recovered energy charges the two capacitors in series. This interval is denoted as interval 4. Owing to the presence of the back electromotive force (EMF) and the battery voltage, the phase current quickly decreases to zero.

In Fig 8(b), the conducting intervals of the incoming phase and outgoing phase are overlapped. *Tc* should be turned on in the excitation interval and demagnetization interval to accelerate the change of current. Therefore, when the phase current in interval 3 overlaps with that in the demagnetization interval of the outgoing phase or initial excitation interval of the incoming phase, the on-state of *Tc* should be kept and the phase voltage turns into 2*Vc*.

IV. Simulation and Experimental Results

In order to validate the proposed integrated topology and control strategy, a topology consisting of a three-phase 35kW SRM and a 50kW load motor is simulated in MATLAB/Simulink and tested experimentally. The rated speed of SRM is 2000 rpm and the peak current of phase A is 200 A. The rated speed of the load motor is 1500 rpm, and the peak power is 100kW. The major parameters of the drive are given in Table I.

TABLE I

SRM and Load Motor Parameters

Parameter	SRM	Load Motor
Phase number	3	3
Rated power (kW)	35	50
Peak power (kW)	60	100
Rated voltage (V)	336	366
Rated speed (rpm)	2000	1500
Rated current (A)	115	140
Stator/rotor poles	12/8	N/A
Cooling method	Natural cooling	Water cooling

A simulation model and a speed control function are established in MATLAB/Simulink. The flux current-position (ψ-*i*-θ) is measured at four specific rotor positions without rotor clamping devices and position sensors. Based on the measured results, the flux-linkage characteristics at any rotor position can be calculated by an analytical expression of flux-linkage.

The simulation results of the battery-alone drive mode and generator-alone drive mode are shown in Figs. 9 and 10. Fig. 9 shows the phase voltage and current simulation waveforms at 500 rpm while a soft-chopping switch method is applied. The supply voltage of the conventional converter is 336 V. The voltages of B1 and B2 are assumed to be 336 V. Meantime, the equivalent source power voltage is set to 336 V in the generator-alone drive mode.

In Fig. 9(a), the demagnetization voltage of a conventional converter is 336V. However, the voltage in battery-alone drive mode is about 670V in Fig. 9(b). The voltage of petrol-alone drive mode is higher, which is about 710V in Fig. 9(c). Since the two capacitors are connected in series, the demagnetization voltage of the battery drive is twice the voltage of the conventional converter. Therefore, the demagnetization time is shorter. A high demagnetization voltage of the two drive operation modes can easily avoid the tail current and reduce the negative torque. In addition, the demagnetization voltage of the generator drive mode is the highest so that the demagnetization time is the shortest, as a result of using a boost circuit and a switch capacitor.

Fig. 10 displays the waveforms of simulation results at 2500 rpm. Due to a high EMF at high speeds, a higher voltage in the two drive operation modes can improve the torque and extend the constant torque range. The torque waveforms of asymmetrical half-bridge are distorted.

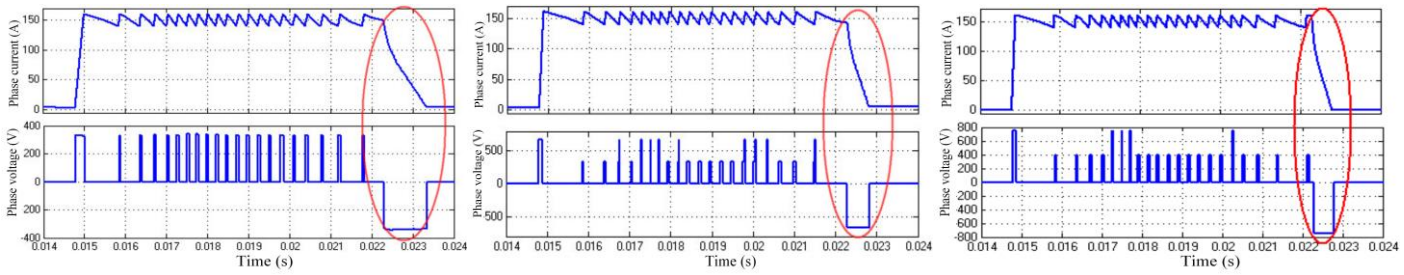

(a) Asymmetrical half-bridge (b) Battery-alone drive mode (c) Generator-alone drive mode

Fig. 9. Simulation results of phase current and voltage at 500 rpm.

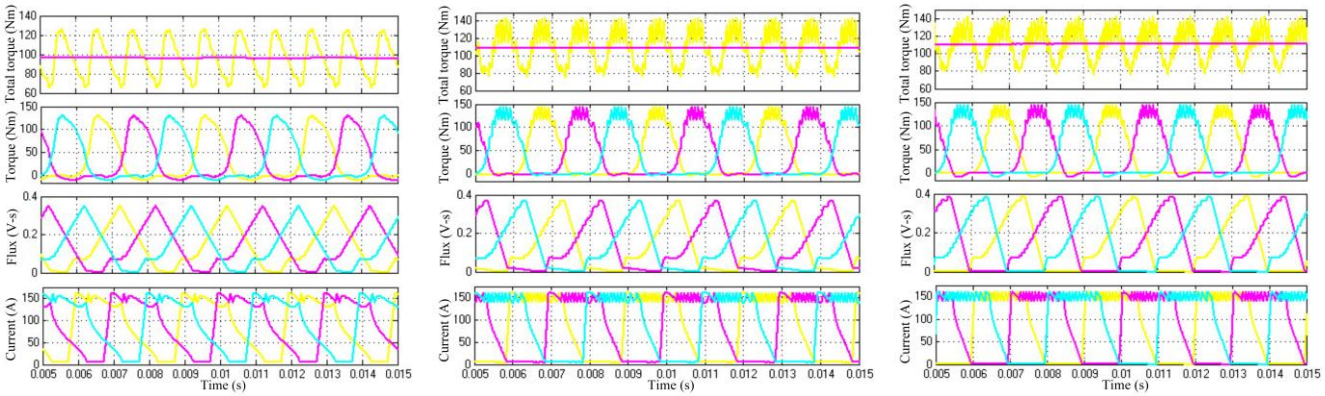

(a) Asymmetrical half-bridge (b) Battery-alone drive mode (c) Generator-alone drive mode

Fig. 10. Simulation results at 2500 rpm.

The transient rotor speed and phase current under acceleration/deceleration conditions are obtained when the motor drive operates in battery-alone drive mode and generator-alone drive mode, as presented in Fig. 11. The simulation results reflect that the proposed motor drive has fast response to the speed variations owing to its excellent excitation and demagnetization capabilities by means of increasing the rotor voltage, which is naturally realized by choosing the operation modes of two capacitors or battery packs in series connection.

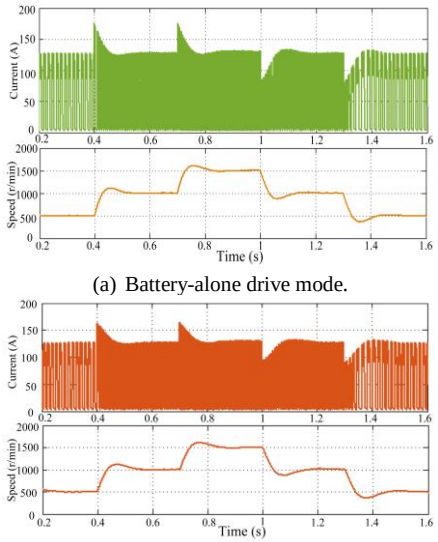

(a) Battery-alone drive mode.

(b) Generator-alone drive mode.

Fig. 11. Simulation results under acceleration/deceleration conditions.

In order to further validate the proposed drive and control strategy, an experimental test rig is set up, as shown in Fig. 12. The major parameters of SRM and drag motor are listed in table I above. The source power voltage is set to 336 V. In addition, a real-time digital simulator, RT-LAB OP5600, is employed to simulate the new converter topology in the experiment. RT-LAB is a distributed real-time simulation platform. RT-LAB is widely applied in hardware-in-the-loop (HIL) simulation for system integration, design, verification and test. It is used to generate output PWM and feedback signals for implementing in real time with a DSP control board.

Fig. 12. Experimental setup.

Figs. 13 and 14 show the experiment results of the battery-alone drive mode and generator-alone drive mode at 500 and 2500 rpm, respectively. In Fig. 9, a high negative voltage during demagnetization can reduce the commutation time and increase the maximum output torque. In the experiments, the demagnetization time of the asymmetrical half-bridge is the longest. The maximum output torque in the battery-alone drive mode is 128.5Nm while the maximum output torque of the asymmetrical half-bridge is 123.2Nm. Moreover, the maximum output torque of the generator-alone drive mode is 135.6Nm, which is also higher than that of the asymmetrical half bridge. The torque ripple of the asymmetrical half-bridge is 121.7%, while the torque ripples of the generator-alone and battery-alone drive modes are 100% and 86.1% respectively. Clearly, the proposed topology can better reduce the torque ripple than traditional asymmetrical half-bridge converters. In Fig. 14, the maximum output torque of the asymmetrical half-bridge is 104.5Nm, and that of the battery-alone drive mode and generator-alone drive mode is 119.5 and 117.9Nm, respectively. It is noted that the maximum output torque in the battery-alone drive mode and generator-alone drive mode are higher than those in the conventional converters in the high speed range. Moreover, the EMF is higher when the SRM operates at 2500 rpm. Hence, the excitation and demagnetization voltages are limited by the source power voltage in conventional SR drives. Also shown in Fig. 14(a) is a normal chopping sequence. Its waveform at high speeds cannot be held, and the current waveform is peculiar. As displayed in Fig. 14(b)-(c), normal chopping waves are kept by the waveforms of battery-alone drive mode and generator-alone drive mode at 2500 rpm. Therefore, the constant torque region in the two modes is longer, indicating better drive performance.

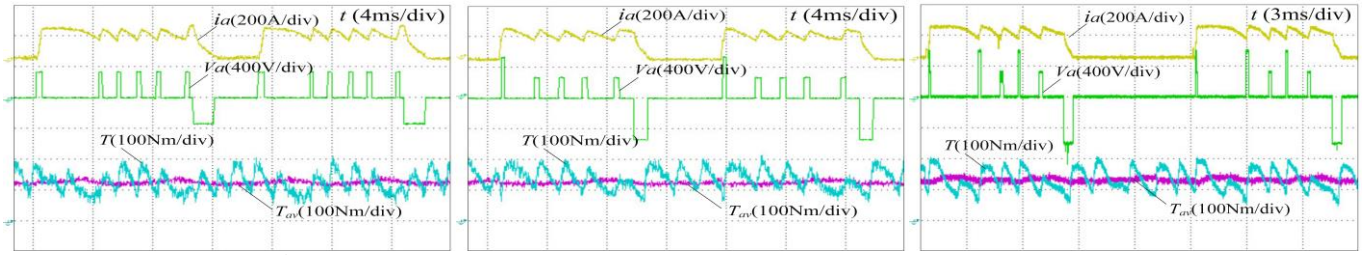

(a) Asymmetrical half-bridge (b) Battery-alone drive mode (c) Generator-alone drive mode

Fig. 13: Compared experiment results (500 r/min).

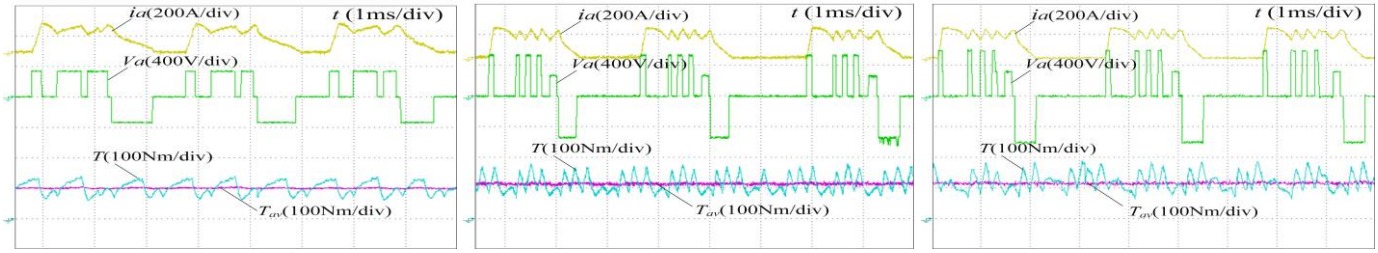

(a) Asymmetrical half-bridge (b) Battery-alone drive mode (c) Generator-alone drive mode

Fig. 14: Compared experiment results (2500 r/min).

Fig. 15 presents the acceleration/deceleration transient response in a closed-loop system, with an enlarged view of abrupt speed changes. It can be seen that the instantaneous speed follows the given speed values well in the battery-alone and generator-alone drive modes. For instance, when the speed suddenly reduces from 1500 to 1000 r/min, the instantaneous speed follows it quickly in 180 ms, and the respond time of battery-alone drive mode is similar to that of generator-alone drive mode. Therefore, the satisfactory speed dynamic responses are verified from the results.

In addition, when relays J_1, J_2 and J_3 are closed, the converter works in the hybrid drive mode or generator drive charging mode according to the load conditions. The difference between the two modes is simply that the battery packs work in either charging or discharging mode. Simulation and experimental results for the two modes are similar to those derived in battery-alone drive mode and generator-alone drive mode. Due to limited space, no more details are discussed here.

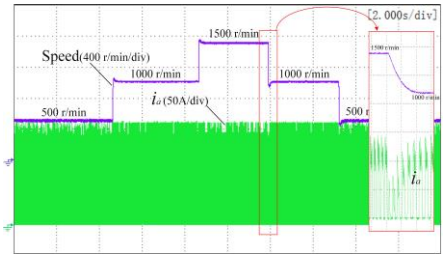

(a) Battery-alone drive mode

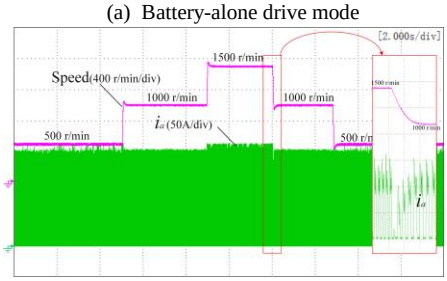

(b) Generator-alone drive mode

Fig. 15: Experimental results under acceleration/deceleration conditions.

Furthermore, the difference between the two kinds of charging modes, where the battery is charged by generator and by external power source, is that the charging source is AC grid or generator. No matter which one of the two charging modes is applied, an equivalent simple boost charging circuit is depicted in Fig. 6. As for the SRM output characteristics, the charging circuit plays an insignificant role from simulation and experimental results. Therefore, due to the similarity between battery-alone drive mode and generator-alone drive mode, no more details are discussed repeatedly.

V. Conclusion

In this paper, a new integrated SRM topology for PHEVs is proposed. Since different working conditions and driving requirements are considered, a varied winding voltage is very essential. From the simulation and experimental results, a high excitation and a high demagnetization voltage in the battery-alone drive mode and generator-alone drive mode can increase the maximum output torque by 14.9% and 13.3%, respectively. Compared to the asymmetrical half-bridge, the torque ripple in battery-alone drive mode or generator-alone drive mode is lower. The asymmetrical half-bridge can operate at low speeds but cannot meet the demand of current chopping control at high speeds. Nonetheless, the proposed topology can work properly in all scenarios, especially in extended constant torque range.

The front end of the proposed topology provides series or parallel connection of two battery packs (or the two capacitors) in order to realize high voltage or high current output. This flexible output characteristic satisfies different working conditions and capacity requirements. Simulation models have been built and experimental results have been obtained to verify the effectiveness of the proposed topology.

References

[1] P. Fajri, M. Ferdowsi, N. Lotfi, and R. Landers, "Development of an Educational Small-Scale Hybrid Electric Vehicle (HEV) Setup," *IEEE Trans. Intell. Transp. Syst.*, vol. 8, no. 2, pp. 8-21, Summer 2016.

[2] M. Shahverdi, M. S. Mazzola, Q. Grice, and M. Doude, "Pareto Front of Energy Storage Size and Series HEV Fuel Economy Using Bandwidth-Based Control Strategy," *IEEE Trans. Transp. Electr.*, vol. 2, no. 1, pp. 36-51, March 2016.

[3] Kim, H. Hwang, S. Bae, and C. Lee, "Analysis and Design of a Double-Stator Flux-Switching Permanent Magnet Machine Using Ferrite Magnet in Hybrid Electric Vehicles," *IEEE Trans. Magn.*, vol. 52, no. 7, pp. 1-4, July 2016.

[4] B. K. Bose, "Global Energy Scenario and Impact of Power Electronics in 21st Century," *IEEE Trans. Ind. Electron.*, vol. 60, no. 7, pp. 2638-2651, July 2013.

[5] P. Fajri, M. Ferdowsi, N. Lotfi, and R. Landers, "Development of an Educational Small-Scale Hybrid Electric Vehicle (HEV) Setup," *IEEE Trans. Intell. Transp. Syst.*, vol. 8, no. 2, pp. 8-21, Summer 2016.

[6] K. Kiyota and A. Chiba, "Design of Switched Reluctance Motor Competitive to 60-kW IPMSM in Third-Generation Hybrid Electric Vehicle," *IEEE Trans. Ind. Appl.*, vol. 48, no. 6, pp. 2303-2309, Nov.-Dec. 2012.

[7] K. Kiyota, T. Kakishima, A. Chiba, and M. A. Rahman, "Cylindrical Rotor Design for Acoustic Noise and Windage Loss Reduction in Switched Reluctance Motor for HEV Applications," *IEEE Trans. Ind. Appl.*, vol. 52, no. 1, pp. 154-162, Jan.-Feb. 2016.

[8] M. Takeno, A. Chiba, N. Hoshi, S. Ogasawara, M. Takemoto, and M. A. Rahman, "Test Results and Torque Improvement of the 50-kW Switched Reluctance Motor Designed for Hybrid Electric Vehicles," *IEEE Trans. Ind. Appl.*, vol. 48, no. 4, pp. 1327-1334, July-Aug. 2012.

[9] Z. Yang, F. Shang, I. P. Brown, and M. Krishnamurthy, "Comparative Study of Interior Permanent Magnet, Induction, and Switched Reluctance Motor Drives for EV and HEV Applications," *IEEE Trans. Transp. Electr.*, vol. 1, no. 3, pp. 245-254, Oct. 2015.

[10] S. Haghbin, K. Khan, S. Zhao, M. Alakula, S. Lundmark, and O. Carlson, "An Integrated 20-kW Motor Drive and Isolated Battery Charger for Plug-In Vehicles," *IEEE Trans. Power Electron.*, vol. 28, no. 8, pp. 4013-4029, Aug. 2013.

[11] S. Song, S. Chen and W. Liu, "Analytical Rotor Position Estimation for SRM Based on Scaling of Reluctance Characteristics From Torque-Balanced Measurement," *IEEE Transactions on Industrial Electronics*, vol. 64, no. 5, pp. 3524-3536, May 2017.

[12] W. Ding, Y. Hu and L. Wu, "Investigation and Experimental Test of Fault-Tolerant Operation of a Mutually Coupled Dual Three-Phase SRM Drive Under Faulty Conditions," *IEEE Transactions on Power Electronics*, vol. 30, no. 12, pp. 6857-6872, Dec. 2015.

[13] J. Cai and Z. Deng, "A Joint Feature Position Detection-Based Sensorless Position Estimation Scheme for Switched Reluctance Motors," *IEEE Transactions on Industrial Electronics*, vol. 64, no. 6, pp. 4352-4360, June 2017.

[14] A. K. Jain and N. Mohan, "SRM power converter for operation with high demagnetization voltage," *IEEE Trans. Ind. Appl.*, vol. 41, no. 5, pp. 1224-1231, Sept.-Oct. 2005.

[15] J. Liang, G. Xu, D. H. Lee, and J. W. Ahn, "Classification of capacitive type converter topologies for SRM," in *Proc. Annu. Conf. IEEE Electr. Mach. and Syst.*, Incheon, 2010, pp. 1670-1675.

[16] H. C. Chang and C. M. Liaw, "An Integrated Driving/Charging Switched Reluctance Motor Drive Using Three-Phase Power Module," *IEEE Trans. Ind. Electron.*, vol. 58, no. 5, pp. 1763-1775, May 2011.

[17] Y. J. Lee, A. Khaligh, and A. Emadi, "Advanced Integrated Bidirectional AC/DC and DC/DC Converter for Plug-In Hybrid Electric Vehicles," *IEEE Trans. Veh. Technol.*, vol. 58, no. 8, pp. 3970-3980, Oct. 2009.

[18] W. Cai and F. Yi, "An Integrated Multiport Power Converter With Small Capacitance Requirement for Switched Reluctance Motor Drive," *IEEE Trans. Power Electron.*, vol. 31, no. 4, pp. 3016-3026, April 2016.

[19] F. Yi and W. Cai, "A Quasi-Z-Source Integrated Multiport Power Converter as Switched Reluctance Motor Drives for Capacitance Reduction and Wide-Speed-Range Operation," *IEEE Trans. Power Electron.*, vol. 31, no. 11, pp. 7661-7676, Nov. 2016.

[20] H. C. Chang and C. M. Liaw, "Development of a Compact Switched-Reluctance Motor Drive for EV Propulsion With Voltage-Boosting and PFC Charging Capabilities," *IEEE Trans. Veh. Technol.*, vol. 58, no. 7, pp. 3198-3215, Sept. 2009.

[21] C. Zhang, K. Wang, S. Zhang, X. Zhu, and L. Quan, "Analysis of Variable Voltage Gain Power Converter for Switched Reluctance Motor," *IEEE Trans. Appl. Supercond.*, vol. 26, no. 7, pp. 1-5, Oct. 2016..

[22] C. Gan, J. Wu, Y. Hu, S. Yang, W. Cao, and J. M. Guerrero, "New Integrated Multilevel Converter for Switched Reluctance Motor Drives in Plug-in Hybrid Electric Vehicles With Flexible Energy Conversion," *IEEE Trans. Power Electron.*, vol. 32, no. 5, pp. 3754-3766, May 2017.

[23] A. C. Oliveira, C. B. Jacobina, A. M. N. Lima, and F. Salvadori, "Startup and Fault Tolerance of the SRM Drive with Three-Phase Bridge Inverter," in *Proc. IEEE 36th Power Elect. Spec. Conf.*, Recife, 2005, pp. 714-719.

[24] J. D. Widmer, B. C. Mecrow, C. M. Spargo, R. Martin, and T. Celik, "Use of a 3 phase full bridge converter to drive a 6 phase switched reluctance machine," in *Proc. IET 6th Power Elect. Mach. Drives Conf.*, Bristol, 2012, pp. 1-6.

[25] X. D. Xue, K. W. E. Cheng, and Y. J. Bao, "Control and Integrated Half Bridge to Winding Circuit Development for Switched Reluctance Motors," *IEEE Trans. Ind. Informat.*, vol. 10, no. 1, pp. 109-116, Feb. 2014.

[26] Xu Deng, B. Mecrow and S. Gadoue, "A novel converter topology for 6 phase switched reluctance motor drives," in *Proc. Annu. Conf. 39th IEEE Ind. Elect. Society*, Vienna, 2013, pp. 268-273.

[27] A. Deriszadeh, E. Adib, H. Farzanehfard, and S. M. Saghaeian Nejad, "Switched reluctance motor drive converter operating in continuous conduction mode with high demagnetisation voltage," *IET Power Electron.*, vol. 8, no. 7, pp. 1119-1127, Jul 2015.

[28] Liang Jianing, Lee Dong-Hee, Xu Guoqing, and Ahn Jin-Woo, "Analysis of Passive Boost Power Converter for Three-Phase SR Drive," *IEEE Trans. Ind. Electron.*, vol.57, no.9, pp. 2961-2971, 2010.

[29] A. Hava, V.Blasko, and T.A. Lipo, "A modified C-dump converter for variable-reluctance machines," *IEEE Trans. Ind. Appl.*, pp. 1017–1022,(1992).

[30] K. Tomczewski and K. Wrobel, "Improved C-dump converter for switched reluctance motor drives," *IET Power Electron.*, vol. 7, no. 10, pp. 2628–2635, 2014.

[31] Y. Hu, X. Song, W. Cao, and B. Ji, "New SR drive with integrated charging capacity for plug-in hybrid electric vehicles (PHEVs)" *IEEE Trans. Ind. Electron.*, vol. 61, no. 10, pp. 5722- 5731, Oct. 2014.

[32] N. Nakao and K. Akatsu, "A simple unipolar excitation strategy for switched reluctance motors by using PWM current control," in *Proc. Annu. Conf.*, Melbourne, VIC, pp. 1111-1117, 2013.

[33] S. Vukosavic and V. R. Stefanovic, "SRM inverter topologies: a comparative evaluation," *IEEE Trans. Ind. Appl.*, vol. 27, no. 6, pp. 1034-1047, Nov/Dec 1991.

[34] H. Chen, G. Han, W. Yan, S. Lu, and Z. Chen, "Modeling of a Switched Reluctance Motor Under Stator Winding Fault Condition," *IEEE Trans on Appl. Supercond.*, vol. 26, no. 4, pp. 1-6, June 2016.